

<https://doi.org/10.1038/s41612-025-01146-1>

# Recent changes in spatiotemporal patterns of heat extremes in South Asia



Abhirup Banerjee<sup>1,11</sup> , Shraddha Gupta<sup>2,3,11</sup> , Pranava Priyanshu<sup>4</sup>, Ankan Kar<sup>5</sup>, Ruby Saha<sup>6</sup>, Tanujit Chakraborty<sup>7,8</sup> , Dibakar Ghosh<sup>4</sup>, Jürgen Kurths<sup>3,9</sup> & Chittaranjan Hens<sup>10</sup>

The likelihood of intense heatwaves in South Asia is increasing due to climate change, highlighting the need to understand their evolving spatiotemporal patterns. Using a complex network-based approach, we analyze synchronous extreme heat events across South and West Asia over three 30-year periods: two historical phases (1960–1989, 1990–2019) and a near-future projection (2020–2049) under the SSP2-4.5 scenario. Our findings reveal a shift in heatwave synchronization from western and central Asia before 1990 towards Pakistan, northwest India, and the southwestern Tibetan Plateau by the mid-21st century. This shift is primarily driven by increased surface sensible heat flux, which enhances atmospheric diabatic heating and strengthens the early-summer circumglobal teleconnection. Additionally, atmospheric conditions over the North Atlantic-Greenland sector modulate South Asian heatwave synchronization. Our study provides novel insights into the evolving land-atmosphere interactions driving extreme heat events, with implications for heatwave predictability and risk assessment in a warming world.

The Sixth Assessment Report of the Intergovernmental Panel on Climate Change confirmed with high confidence that the rising trend of heat extremes across most of Asia is projected to continue in the coming decades<sup>1</sup>. Climate change has amplified droughts in the arid and semi-arid regions of western, central, and southern Asia and increased the likelihood of spring to summer heatwaves (HWs) across the continent<sup>2</sup>. In India, HWs occur frequently during the pre-monsoon season (March to May, extending into mid-June until the onset of monsoon), primarily affecting the northern and central regions<sup>3</sup>. Recent data indicates a rise in HWs in northern Pakistan, northwest India, the Indo-Gangetic Plain, and the Tibetan Plateau (Fig. 1). South Asia is one of the most susceptible regions to climate extremes due to its diverse landscape, varied climate, high population density, rapid urbanization, and limited adaptive capacity. This region alone accounted for 23% of the 489,000 annual global heat-related deaths between 2000 and 2019<sup>4,5</sup>. Extreme heat conditions also severely impact agriculture, causing crop damage, yield reductions, and socio-economic decline<sup>6,7</sup>. Cascading effects of heat extremes can increase susceptibility to wildfires, extreme rainfall, flooding due to enhanced snowmelt and soil erosion, often leading to compound events<sup>8–13</sup>.

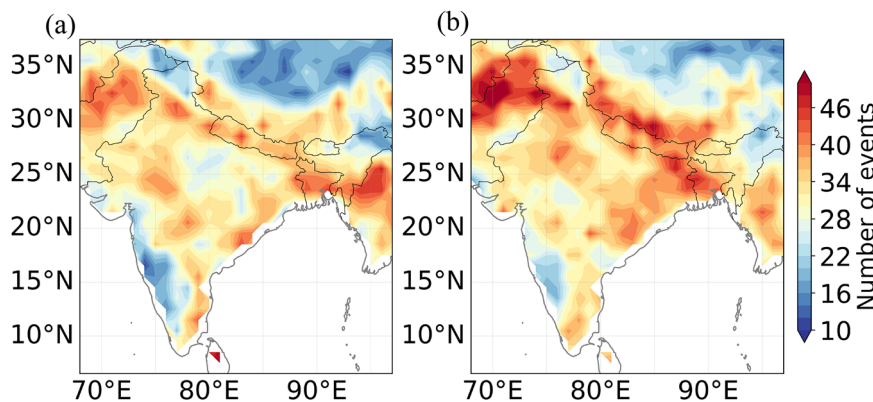
In South Asia, HWs can develop and persist due to the simultaneous occurrence of multiple favorable conditions. These conditions arise from a complex interplay of local and remote factors. Regionally, persistent high-pressure systems lead to atmospheric blocking, causing air to descend (subsidence), resulting in clear skies and higher surface temperatures. Dry soil further intensifies the heat by limiting evapotranspiration<sup>14,15</sup>.

At larger scales, the amplified phases of the atmospheric circumglobal teleconnection (CGT), a wave-like pattern that travels along the mid-latitude jet, can trigger high-pressure systems over South Asia, leading to blocking events and stationary Rossby wave propagation<sup>16–18</sup>. Further, studies have linked anomalous anticyclonic circulation over the North Atlantic and anomalous Atlantic sea surface temperatures to high-pressure anomalies over northern India<sup>14,19,20</sup>. Anomalous European lows can produce blocking highs over north India and Pakistan, often associated with a weakened polar jet stream and a northward-shifted subtropical jet, thereby promoting pre-monsoon HW development<sup>21,22</sup>.

Although several works have examined decadal variations and future trends in the frequency, persistence, and spatial classification of Indian HWs<sup>23–25</sup>, limited attention has been given to understanding the recent

<sup>1</sup>Institute of Oceanography, University of Hamburg, Hamburg, Germany. <sup>2</sup>Department of Geography, Ludwig-Maximilians-Universität München, Munich, Germany. <sup>3</sup>Potsdam Institute for Climate Impact Research (PIK)—Member of the Leibniz Association, Potsdam, Germany. <sup>4</sup>Indian Statistical Institute, Kolkata, India. <sup>5</sup>Department of Computer Science, Chennai Mathematical Institute, Tamil Nadu, India. <sup>6</sup>Department of Physics, Indian Institute of Technology Madras, Chennai, India. <sup>7</sup>Department of Science and Engineering, Sorbonne University, Abu Dhabi, United Arab Emirates. <sup>8</sup>Sorbonne Center for Artificial Intelligence, Sorbonne University, Paris, France. <sup>9</sup>Department of Physics, Humboldt University at Berlin, Berlin, Germany. <sup>10</sup>Center for Computational Natural Science and Bioinformatics, International Institute of Informational Technology, Hyderabad, India. <sup>11</sup>These authors contributed equally: Abhirup Banerjee, Shraddha Gupta. e-mail: abhirup.banerjee@uni-hamburg.de; shraddha.gupta@lmu.de; tanujit.chakraborty@sorbonne.ae; kurths@pik-potsdam.de

**Fig. 1 | Number of heatwaves during over South Asia during the pre-monsoon season across historical periods.** Heatwaves during March–April–May (see definition in Heatwave identification in “Methods”) were identified using ERA5 daily 2m-temperature for the periods: **a** 1960–1989 and **b** 1990–2019. Each grid point shows the total number of heatwave events over the respective 30-year span. Warmer colors indicate higher frequency.



changes in their spatiotemporal coherence patterns arising due to related large-scale drivers. Understanding these changes is crucial for effective risk assessment and management, given South Asia’s significant socioeconomic vulnerability to climate impacts. Furthermore, examining changes in land-atmospheric processes that contribute to more frequent and intense HWs is especially relevant in the context of anthropogenic land use and land cover changes over the decades<sup>26,27</sup>. Such insights are essential for improving model accuracy and enhancing predictive capabilities. For example, HWs affecting Pakistan and northern India in recent years could be predicted well in advance in extended-range forecasts, but the mechanisms underlying this predictability have remained unclear<sup>28</sup>.

This study investigates interdecadal changes in the interannual variability of the spatiotemporal patterns of spring (March–April–May) extreme heat events across South Asia, as well as adjacent regions in Central and West Asia, which exhibit related mechanisms leading to synchronous heat events. However, traditional methods such as correlation analyses, empirical orthogonal functions, and seasonal composites used in previous studies have limitations in capturing spatial extreme heat covariability<sup>29</sup>. To gain insight into the spatiotemporal dynamics of HWs, we employ the framework of climate networks. This belongs to the class of functional complex networks, wherein the nodes represent geographical locations and the edges represent the similarities between their dynamical behavior (see Functional network construction using event synchronization in “Methods”)<sup>30</sup>. To assess the similarity between HW events at different locations, we use an event-based nonlinear similarity measure, known as event synchronization (ES)<sup>31,32</sup>. The integration of ES with complex network theory has proven to be highly effective in revealing global and regional coupling patterns of extreme climate events, such as precipitation<sup>33,34</sup>, heatwaves<sup>35,36</sup>, and droughts<sup>37,38</sup>, allowing the identification of specific large-scale atmospheric circulations associated with synchronous extreme events<sup>32,39</sup>.

The primary interest of our study is to identify continental-scale coherence patterns of HWs in South Asia and understand their evolution over multiple climatological periods. To achieve this, we integrate historical temperature data from ERA5 reanalysis and CMIP6 future projections from three Earth System Models, namely MPI-ESM1.2-LR, CNRM-CM6-1 and UKESM1-0-LL (see Data in “Methods”). Previous studies have identified a structural change in temperature trends and circulation patterns around the mid-1990s<sup>22,40,41</sup>. Accordingly, we divide the historical period of analysis into two equal 30-year climatological periods: 1960–1989 (P1) and 1990–2019 (P2), selecting 1990 as a practical cutoff to ensure comparability and temporal symmetry. This division also aligns with broader climatic and socio-economic transitions in South Asia during the post-1990 period, such as accelerated urbanization, land-use change, and increased greenhouse gas emissions<sup>1,42–44</sup>. Furthermore, to understand how HW coherence patterns may evolve further under a realistic future warming scenario (SSP2-4.5) with moderate emissions given current policies, we analyze near-future temperature projections from CMIP6. For consistent temporal comparison

across past and projected climates, we also use a 30-year window for the future period (2020–2049).

HW events are defined as daily temperature anomalies, with respect to the climatology of the given period, exceeding one standard deviation for at least five consecutive days (refer to the definition in Heatwave identification in “Methods”). Using event synchronization-based complex network architecture and network-derived composite analysis, we identify changes in land atmospheric processes associated with synchronous HWs in each climatological period. Comparing two historical 30-year periods instead of a single long historical period, along with future projections, allows us to study the evolution of HW characteristics over time and assess multi-decadal variability. This approach enables us to identify the most susceptible regions to synchronized heat extremes in a progressively warming climate, along with the potential factors contributing to South Asian HW development. Finally, we use causal network analysis to examine changes in the causal interrelationships among these factors in the recent decades and validate our findings (see Causal network analysis in “Methods”). Such an interdecadal comparison enables us to unravel changes in the interplay of different factors influencing South Asian HW development post-1990 warming (see “Results”).

## Results

### Heatwave coherence patterns in different climatological periods

We compare the spatiotemporal synchronization pattern of March–April–May HWs over the Indian subcontinent of two different historical climatological periods (see Fig. 1) using the node-based network centrality measure *degree* as shown in Fig. 2 (see Functional Network Construction using Event Synchronization and Network measures in “Methods”). We choose the maximum allowed delay as  $\tau_{\max} = 5$  days to identify synchronized events. This choice is motivated by the typical lifetime of synoptic-scale atmospheric systems—such as blocking highs and Rossby wave trains—that are known drivers of heatwaves and generally persist for 5 to 7 days<sup>45,46</sup>. Selecting  $\tau_{\max}$  within this range allows us to capture synchronization between events likely influenced by the same large-scale system, while avoiding spurious associations with unrelated events.

For both P1 and P2 (1960–1989 and 1990–2019 respectively), a significantly high-degree interaction is observed in the regions covering northwest and central parts of India, most of Pakistan, the Himalayas, and the Tibetan Plateau. There is a striking increase in the connectivity pattern during P2 (Fig. 2b) in these high-degree regions compared to P1 (Fig. 2a). The degree distribution of the network for 1990–2019 (P2) extends to higher values and exhibits a thicker tail compared to 1960–1989 (P1), reflecting an increase in node connectivity and heterogeneity in the spatial synchronization of extreme heat events (Supplementary Fig. S1). The high-degree regions in our network align closely with areas showing increasing HW trends, consistent with findings reported in previous studies<sup>19,24</sup>. The increase in HW occurrences has been associated with anthropogenic warming<sup>24,47–49</sup>.

**Fig. 2 | Network degree spatial patterns of synchronous heatwaves over South Asia during the pre-monsoon season.** Network degree maps derived from ERA5 daily 2m-temperature during March-April-May, capturing synchronous heatwave occurrences with maximum allowed temporal delay of  $\tau_{\max} = 5$  days for the span: **a** 1960–1989, and **b** 1990–2019. Higher degree values indicate regions with more frequent synchronous heatwave connections to other grid points in the network.

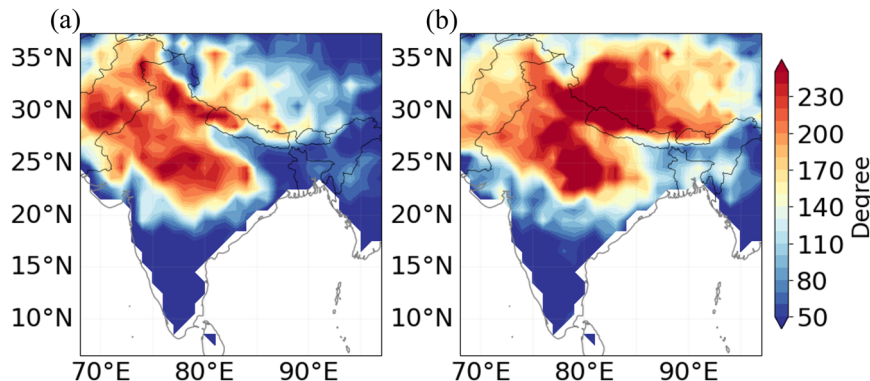
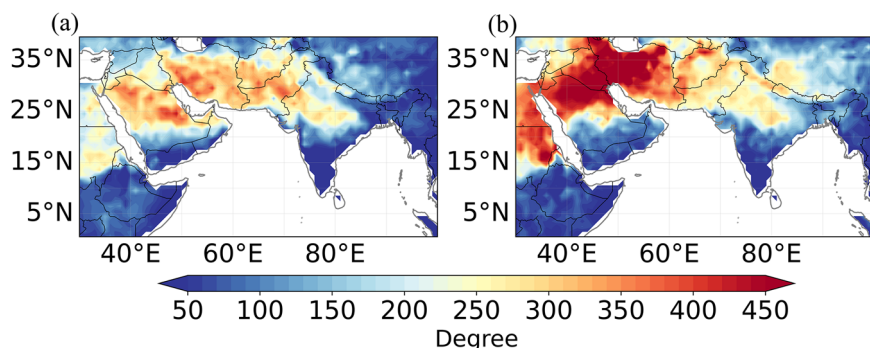


**Fig. 3 | Network degree spatial patterns of synchronous heatwaves over South and West Asia during March–April–May.** Network degree maps derived from ERA5 daily 2m-temperature, capturing synchronous heatwave occurrences with maximum allowed temporal delay of  $\tau_{\max} = 7$  days for the span: **a** 1960–1989, and **b** 1990–2019. Higher degree values indicate regions with more frequent synchronous heatwave connections to other grid points in the network.



Although HW events occur across the Indian subcontinent (Fig. 1), we find that only those in the northwestern regions of the area under consideration exhibit strong spatial synchronization (Fig. 2). This aligns with the complex network-based findings of ref. 36, in which the authors further infer that the pre-monsoon HWs in India predominantly originate in the northwestern parts of the country before propagating toward the northeast or southeast. However, rather than viewing this as a directional propagation, we argue that the underlying dynamics in the northwest are fundamentally different from those governing HW events in other regions<sup>19,50</sup>. This distinction is evident in the spatial patterns of network degree (Fig. 2). Moreover, our findings suggest that the synchronization of HW events in northwest India may be influenced by external factors originating from West Asia (including the Middle East and Southwest Asia). To gain deeper insight into the physical mechanisms driving this synchronization, it is essential to extend our network analysis further northwestward. Figure 3 shows the network degree patterns of the extended region for both historical climatological periods. In this case, the chosen maximum delay  $\tau_{\max}$  is increased to 7 days to identify synchronized extreme heat events belonging to similar atmospheric dynamics even over longer distances. Although, our results are consistent for  $\tau_{\max} = 5$  days, as demonstrated in Robustness tests in “Methods”.

From the spatial connectivity pattern, it appears that the extreme heat events in northwestern India and Pakistan belong to a larger cluster of synchronized events that extend to Iran, the northern Arabian peninsula, and northeastern Africa (Fig. 3). We reveal that there is an overall significant enhancement in the synchronization of heat events in these regions during P2 compared to P1 (compare Fig. 3b and a, respectively).

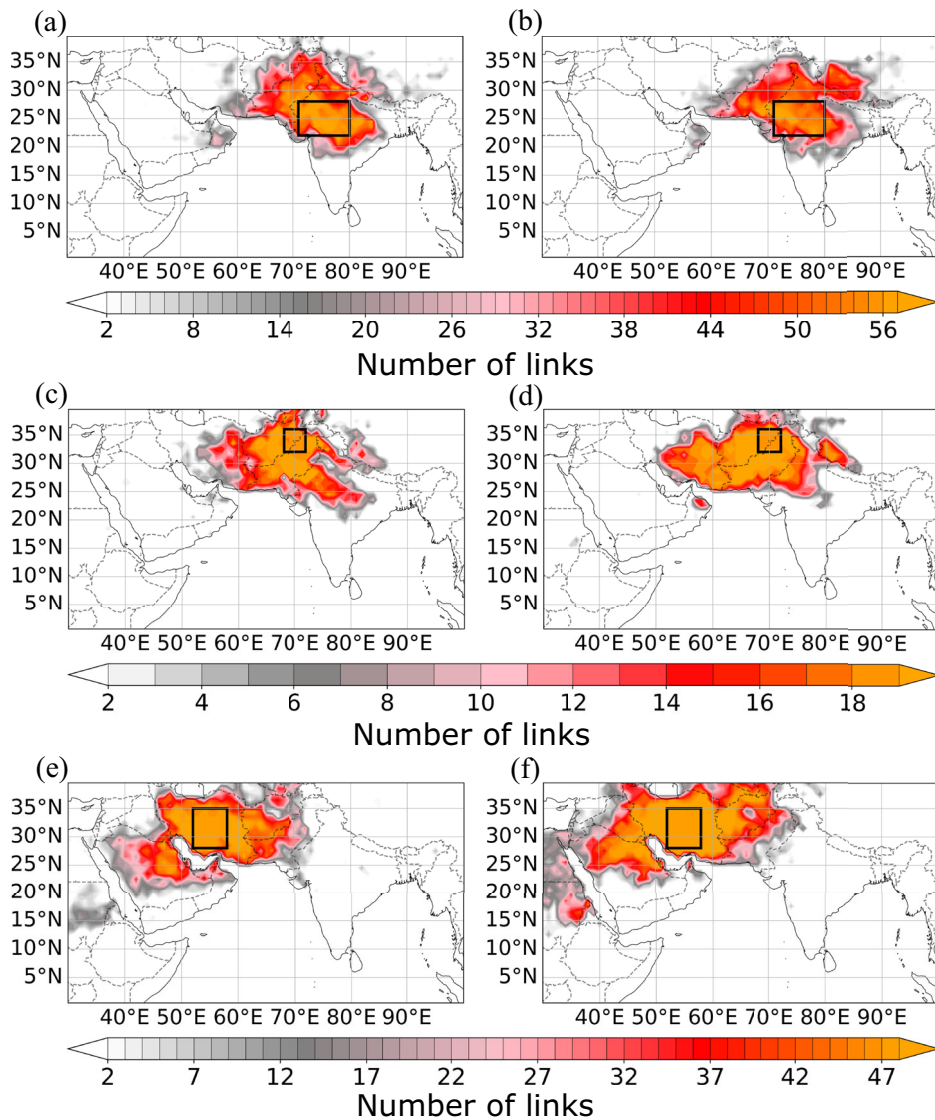
In order to confirm this, we compute the partial degree (see equation (3) under subheading Network measures of “Methods”) of selected high-degree regions, namely, northwestern India, northwestern Pakistan, and Iran, for both historical periods. This measure decomposes the total network degree for each region, allowing us to quantify how their connectivity to other areas has evolved over time (Fig. 4). The use of partial degree thus

offers a finer-grained view of network structure, revealing changes in regional linkages that are not apparent in the more aggregated degree maps of Fig. 3. We find that northwest India exhibits high connectivity to most of Pakistan, eastern Afghanistan, the southwestern Tibetan plateau, southeast Iran, and parts of the Indo-Gangetic Plain during both P1 and P2 (Fig. 4a, b). However, in P2, this region shows increased synchronization with the southwestern Tibetan plateau and Pakistan, but reduced connectivity to eastern India (compare Fig. 4b to a). Similarly, during P2, Pakistan’s connectivity has not only strengthened westwards—particularly with Iran—but also eastwards, to the Tibetan plateau and northwest India (compare Fig. 4d to c). Iran’s connectivity has also expanded and amplified, both westward and eastward, during the later period P2 (compare Fig. 4f to e).

The spatial connectivity pattern of HWs contrasts sharply with the spatial distribution of the number of extreme heat events (Supplementary Fig. S2) for both historical periods. This distinction arises because the event synchronization network identifies regions with similar event profiles, such as south-central Asia and northwest India, which are likely influenced by related large-scale land-atmosphere processes. Conversely, the synchronization patterns of extreme heat events in eastern and southern India, and the Horn of Africa (Supplementary Fig. S2), do not emerge prominently in the network analysis (Fig. 3), presumably because HWs in these areas are governed by different underlying mechanisms<sup>50</sup>. This underscores the ability of the complex network approach to distinguish between HW regions based on their driving processes.

The observed changes in HW synchronization patterns between the two historical climatological periods are likely associated to the shift in the warming trend after 1990<sup>41</sup>. It is therefore imperative to investigate how these patterns may evolve under future warming scenarios, which we address in the following analysis. Figure 5a, c, e shows the number of projected HW events lasting at least 5 days for the period 2020–2049 under the SSP2-4.5 scenario, as simulated by three CMIP6 models, namely MPI-ESM1.2-LR, CNRM-CM6-1, and UKESM1-0-LL. At the regional scale, MPI-ESM1.2-LR performs moderately well to reproduce large-scale

**Fig. 4 | Comparison between the partial degree patterns for selected regions, derived from the HW networks corresponding to the two historical climatological periods shown in Fig. 3.** Partial degree patterns are shown for regions **a, b** northwest India, **c, d** Pakistan, and **e, f** Iran. The color-shaded areas show the regions which are linked to the area enclosed by the rectangular black box due to synchronous occurrence of extreme heat events.



temperature and precipitation patterns over India and South Asia, and has been used in heatwave assessments<sup>24,51,52</sup>. Among other CMIP6 models, CNRM-CM6-1 performs best to represent the spatial temperature patterns over India while UKESM1-0-LL captures temporal temperature features better<sup>53</sup>. The number of HW events for MPI-ESM1.2-LR and CNRM-CM6-1 (Fig. 5a, c) are comparable to those during P2 in ERA5 (Supplementary Fig. S2b), with increases HWs in South Asia and the Middle East. The spatial distribution of the number of HW events is similar for MPI-ESM1.2-LR and CNRM-CM6-1, except the latter severely underestimates HW events in the Tibetan Plateau due to a large cold bias<sup>54</sup>. UKESM1-0-LL underestimates the number of HW events overall, especially in semi-arid and arid regions (Fig. 5b).

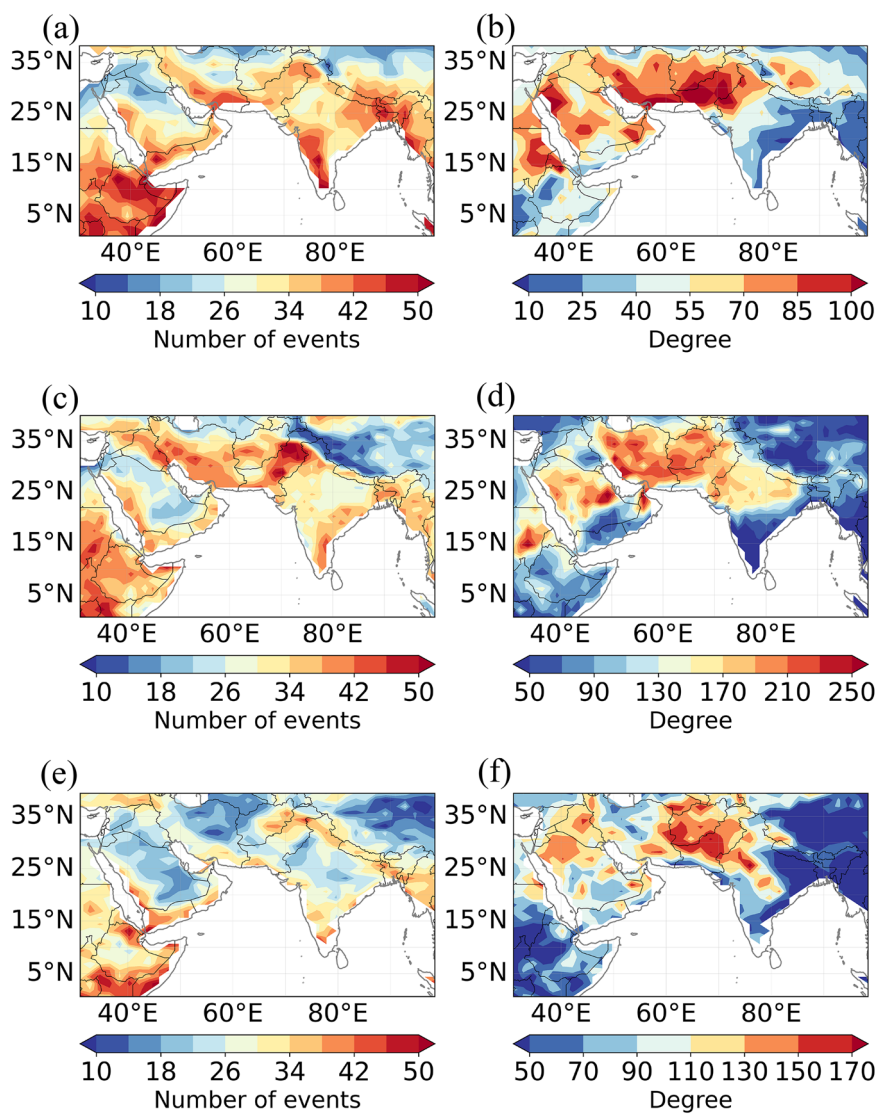
A qualitative comparison of the model-based near-future network degree patterns (Fig. 5b, d, f) with the ERA5 based historical networks (Fig. 3b), reveals a noticeable strengthening in HW synchronization over northern India and Pakistan. High synchronization of extreme heat events is also observed across south western Tibetan Plateau (except CNRM-CM6-1), Iran (less apparent in UKESM1-0-LL), parts of the Arabian Peninsula, and North Africa (except UKESM1-0-LL). However, as the degree of the climate network is proportional to the total number of nodes of the network and, hence, the spatial resolution of the underlying dataset, further quantitative comparisons are needed for a consistent evaluation. To facilitate

resolution-independent spatial analysis, we normalize the network degree of the ERA5 historical periods and the future period of the three CMIP6 models, by  $(N - 1)$ , with  $N$  representing the total number of nodes. The spatial patterns of this normalized metric, called degree centrality (Supplementary Fig. S3), are consistent with the findings drawn from the qualitative comparisons above.

Furthermore, we also compare the networks of model future projections against each model's own historical simulation for the period 1990–2014 (Supplementary Fig. S4). An observation consistent across all models relative to their own baseline is that there is a decrease in connectivity over Iran, but an eastward extension of high-degree regions penetrating more towards Pakistan and northern and central India (and Tibetan Plateau, except in CNRM-CM6).

These findings confirm that regional connectivity has not only strengthened post-1990 but has also undergone spatial reorganization, particularly among Iran, Pakistan, and northwest India—likely reflecting changes in large-scale land-atmosphere processes. The observed eastward shift in the region exhibiting the strongest synchronization of HWs, from West Asia towards India and Tibetan Plateau, in the future climatological period compared to historical periods is likely associated with changes in the underlying physical mechanism of such events. We explore this further in the subsequent analysis.

**Fig. 5 | Projected heatwave frequency and network connectivity patterns under the SSP2-4.5 scenario during 2020–2049.** Future projections from CMIP6 simulations for March–April–May under the SSP2-4.5 scenario are shown for three climate models: **a, b** MPI-ESM1.2-LR, **c, d** CNRM-CM6-1, and **e, f** UKESM1-0-LL. Subfigures (**a, c, e**) show the number of heatwave events, while (**b, d, f**) depict the corresponding network degree patterns constructed with a maximum allowed temporal delay of  $\tau_{\max} = 7$  days.



### Identifying potential drivers of synchronized heat events across periods

We investigate changes in the land-atmospheric processes and circulation patterns related to the high synchronization of extreme heat events between the key regions identified through the functional network analysis. The regions identified through the partial degree analysis are subsequently used as key domains in our composite and causal network analyses: the Iran box (Fig. 4e, f) is labeled as region *IR*, while the adjoining domain over Pakistan and northwest India (Fig. 4a–d) is combined and referred to as region *IN*. These two selected domains are representative of the larger spatial pattern (Fig. 3) and allow us to robustly assess circulation mechanisms associated with regionally synchronized heat extremes. To quantify the climatic factors, we identify days of high synchronization ( $ES_{IR \rightarrow IN}$ ) using ES (see Identification of synchronization days for composite analysis in “Methods”) between the regions *IR* and *IN*, denoted by rectangular black boxes in Figs. 6–8. This yields a list of time indices  $HW_t$  that denote the onset of heat events in *IR* after which there is a HW event in *IN* within  $\tau_{\max} = 7$  days. We center our composite analysis around  $HW_t$ . The period from  $HW_t - 5$  to  $HW_t$  captures the development of land-atmospheric conditions potentially responsible for triggering HWS in *IR*. The subsequent evolution (from  $HW_t$  through  $HW_t + 5$  days) captures how these conditions evolve and propagate, potentially contributing to the later development of HWS in *IN*.

The composites of daily T2m anomalies associated with the synchronization between the *IR* and *IN* regions for both climatological periods (see leftmost column of Figs. 6 and 7) reveal distinct patterns of high-temperature anomalies. In both periods, anomalously high temperatures develop over South Central Asia a few days before  $HW_t$ , intensifying over Iraq and Iran by  $HW_t$ . Approximately five days later, this high-temperature anomaly shifts eastward, resulting in an increase in temperatures over northwest India and Pakistan. However, notable differences emerge between P1 and P2, particularly over India and the Tibetan Plateau.

During P2, the significance of anomalous high T2m is more pronounced over northwest India on  $HW_t$  (compare Figs. 6e and 7e). Furthermore, in  $HW_t + 5$ , while significant high-temperature anomalies are widespread across India during P1, the regions of strong significance are more confined to the northwestern parts of India during P2 (compare Figs. 6i and 7i). Another important difference in P2 is the northward shift of significant temperature anomalies, with an amplified warming over the Tibetan Plateau, further differentiating it from the period P1. This suggests a spatial redistribution and intensification of HW patterns in P2 compared to P1, particularly in northwest India and the Tibetan Plateau, as also observed from the network degree patterns in Fig. 3.

Land-atmospheric processes play a crucial role in modulating the land surface temperatures. Thermal exchange between land and atmosphere, along with persistent atmospheric circulation states, can exacerbate

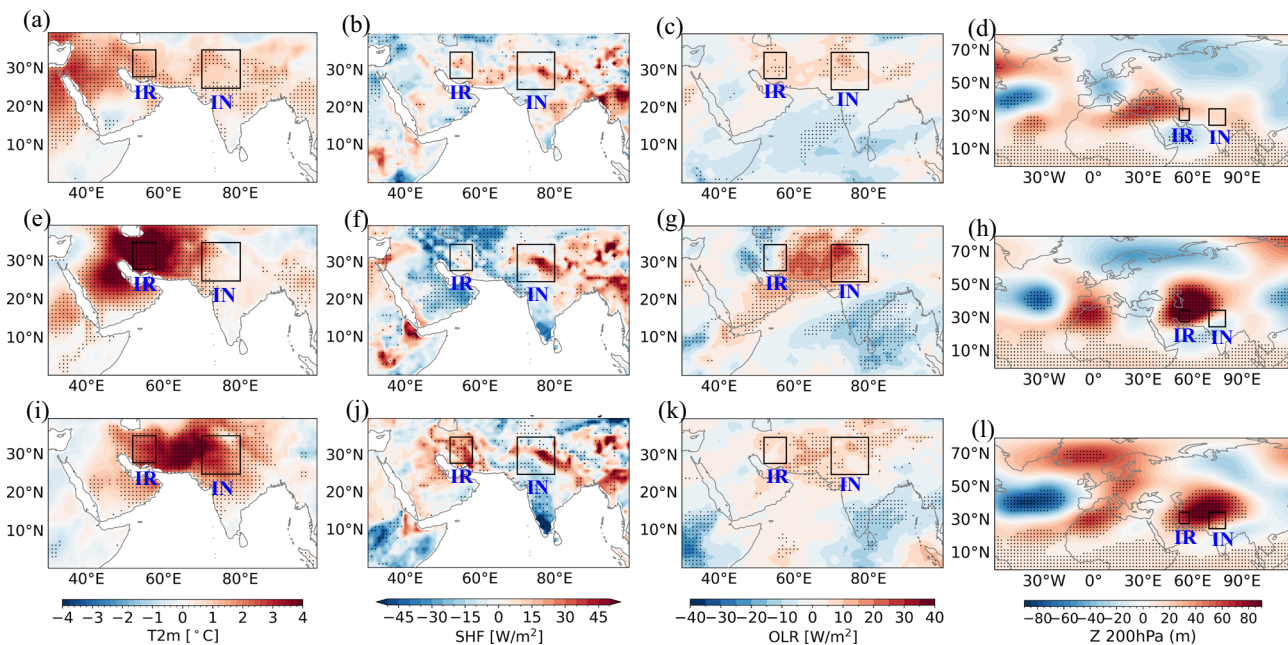


**Fig. 6 |** Composites of daily anomalies of surface 2m-temperature (T2m; *first column from left*), sensible heat flux (SHF; *second column*), outgoing longwave radiation (OLR; *third column*), and geopotential height at 200 hPa (Z200; *fourth column*) for the climatological period 1960–1989, based on the days of high extreme heat synchronization ( $HW_t$ ) between Iran (IR) and northwest India-

(IN) regions in MAM season. Anomaly values are shown using color shading, and the synchronization regions are indicated by rectangular black boxes. Composite anomaly patterns are shown for **a–d** 5 days before  $HW_t$ , **e–h** during  $HW_t$ , and **i–l** 5 days after  $HW_t$ . Black dots denote statistical significance exceeding 95<sup>th</sup> percentile.

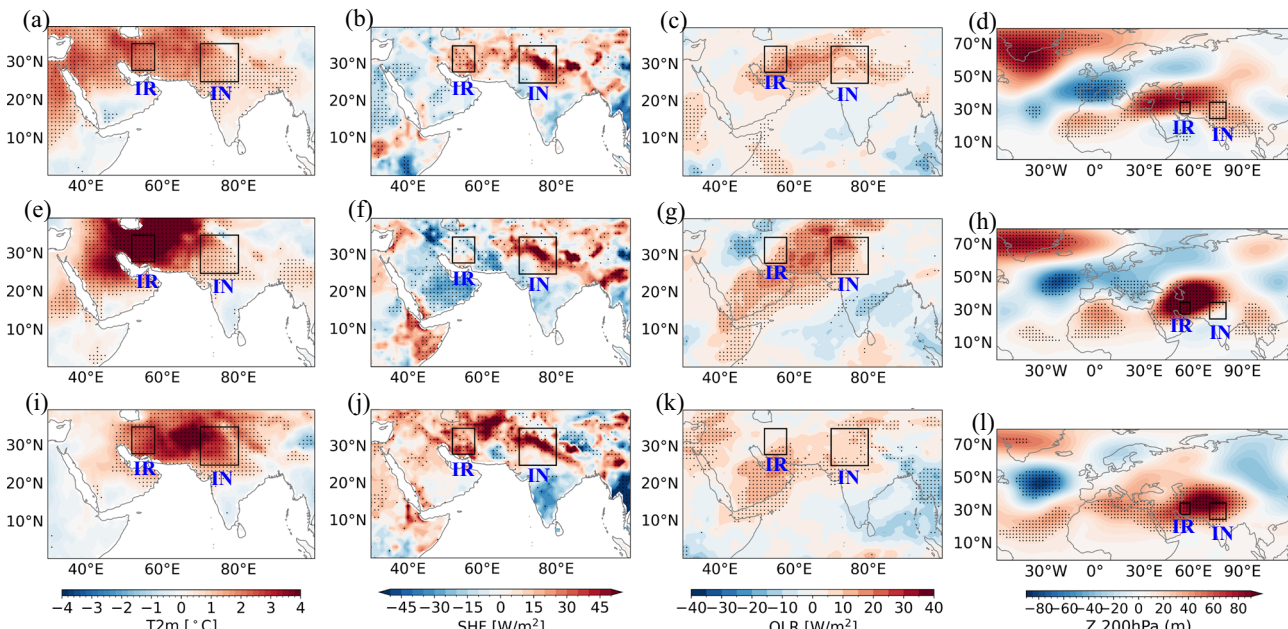


**Fig. 7 |** Composites of daily anomalies of surface 2m-temperature (T2m; *first column from left*), sensible heat flux (SHF; *second column*), outgoing longwave radiation (OLR; *third column*), and geopotential height at 200 hPa (Z200; *fourth column*) for the climatological period 1990–2019, based on the days of high extreme heat synchronization ( $HW_t$ ) between Iran (IR) and northwest India-

(IN) regions in MAM season. Anomaly values are shown using color shading, and the synchronization regions are indicated by rectangular black boxes. Composite anomaly patterns are shown for **a–d** 5 days before  $HW_t$ , **e–h** during  $HW_t$ , and **i–l** 5 days after  $HW_t$ . Black dots denote statistical significance exceeding 95<sup>th</sup> percentile.

HWs<sup>27,55,56</sup>. Before the onset of HWs, we observe positive SHF implying excess energy being transferred as sensible heat due to reduced evapotranspiration. This is likely due to arid soil conditions in these regions, as mentioned in several studies<sup>57</sup>. This process enhances the temperature of the atmosphere by diabatic heating<sup>58</sup> (Figs. 6a, b and 7a, b). Negative SHF

anomalies are observed at the onset of HWs over West Asia and southwest Iran during both P1 and P2 (Figs. 6f and 7f). Increased subsidence during this phase inhibits upward heat transfer, causing heat to be redirected from the atmosphere to the surface and depleting soil moisture. Conversely, positive SHF anomalies appear over northern Pakistan, northern India, and

the Tibetan Plateau at the HW onset ( $HW_t$ ), indicating the developing phase of HWs in these areas. As the HW progresses, an increase in the SHF anomaly is observed over the affected regions, indicating a positive feedback loop between land and atmosphere which increases the persistence of the HW (Figs. 6j and 7j). These anomalies reveal spatial differences in HW progression, inducing distinct regional dynamics in their development.

Although both climatological periods (P1 and P2) show similar HW preconditions as described above, P2 exhibits a notably higher upward SHF anomaly during periods of synchronous HWs in the region (see second column from the left of Figs. 6 and 7). This highlights an intensification in SHF trends across recent decades, likely due to land use and land cover changes in the region such as urbanization, deforestation, desertification, etc.<sup>26</sup>. In P1, two distinct SHF hubs appear during  $HW_t + 5$ —one around southwest of Iran and the northeastern Arabian Peninsula, while the other over northern India, southwestern Tibetan Plateau and adjacent regions (Fig. 6j). This aligns with the high synchronicity hub over West Asia in the network degree pattern of the corresponding period (Fig. 3a), but not over South Asia. In contrast, during P2, a band of enhanced SHF is observed that extends from West Asia to Afghanistan, Pakistan, northern India, and the Tibetan plateau. Notably, the patterns of positive composite anomalies of SHF( $HW_t + 5$ ) in P2, bear a high resemblance to the extreme temperature network degree patterns in Fig. 3, for both P1 and P2. This change in the SHF pattern is reflected in the corresponding network degree pattern in Fig. 3b. This suggests that SHF was a dominant driver of energy transfer from the land to the atmosphere in West Asia during both periods. However, P2 marked a shift in South Asia, where SHF became a major driver of thermal feedback due to the high sensitivity of the atmosphere to land surface drying, potentially prolonging and intensifying HWs. These regions of high SHF anomaly in north India and Pakistan coincide well with regions of strong sensitivity of surface energy fluxes to soil moisture deficits during March-April-May shown in<sup>59</sup>, further supporting our findings.

The increase in SHF prior to HW onset is associated with enhanced diabatic warming, as indicated by significant positive Outgoing Long-wave Radiation (OLR) anomalies and elevated surface temperatures over both IR and IN (Figs. 6c, 7c). An upward OLR directly translates to increased heating because it signifies less cloud cover, allowing more solar radiation to reach and warm the surface. Consequently, the reduced cloud-induced cooling effect further intensifies the heat at the surface. These conditions are especially prominent over India during  $HW_t$  and appear more widespread and intense in P2 (Figs. 6g, 7g) compared to P1. These findings suggest a recent amplification of atmospheric conditions that promote extreme heat events.

An anomalous anticyclonic pressure pattern extending from northwestern Africa towards the east of India is observed before the onset of the HWs for both periods (P1 and P2) (Figs. 6d and 7d). Significant positive instantaneous correlations are observed between SHF and Z200, as well as between OLR and Z200, over regions of high SHF (Supplementary Figs. S5a and S6a). This supports a physically consistent relationship in which surface-driven heating contributes to upper-tropospheric height increases<sup>18</sup>. Over the next few days, a persistent strong ridge develops in the mid-to-upper troposphere over South West Asia (see Z200( $HW_t$ ) and Z500( $HW_t$ ) in Figs. 6h, 7h and Supplementary Fig. S7e–f), which later extends eastward to Pakistan and northwest India (Figs. 6l and 7l). Notably, the region of strongest positive correlation between SHF and Z200 shifts northeastward toward the Tibetan Plateau as the lead time progresses from day 0 to day +4 (Supplementary Fig. S5a–c), aligning with the evolving structure of the regional anticyclone during heatwave development (Figs. 6d,h,l and 7d,h,l). This fosters a conducive environment for the genesis of ‘dry heat wave’<sup>60,61</sup>. This high-pressure system contributes significantly to the development and persistence of HWs by trapping warm air, preventing its dissipation. This induces subsidence, which compresses and warms the air near the surface, further increasing the temperature<sup>27,45,55</sup>. In turn, the subsidence and heat entrapment modify surface energy balances, regulating subsequent SHF and creating a positive feedback loop that sustains the extreme heat conditions (Supplementary Fig. S5d, e).

Although the spatial extent of observed heatwaves in South Asia (Figs. 6i and 7i) exceeds the narrow northwest-southeast high SHF anomaly band in north India-Pakistan regions (second columns of Figs. 6 and 7), these regions closely aligns to regions of positive temperature advection at 850 hPa during the pre-monsoon season<sup>62</sup>. This further suggests that anomalous horizontal advection, associated with large-scale circulation patterns can transport warm air into regions outside the SHF anomaly zone. Thus, we interpret the SHF anomaly band as a land-atmosphere coupling hotspot that may act as a local trigger for heatwave development, with atmospheric feedbacks and heat transport processes facilitating the broader spatial manifestation of heatwaves beyond this core zone.

Previous studies have associated quasi-stationary Rossby wave trains with the occurrence of HWs over northwestern India<sup>14,63</sup>. Our analysis also reveals a similar wave train in composites of upper-level meridional wind (V200) anomalies extending from the Atlantic entry point of the African jet to South Asia during the occurrence of synchronous HWs in the region for both historical periods (Supplementary Fig. S7a, b). This wave train is indicative of the circumglobal teleconnection (CGT) pattern, which is known to facilitate the propagation of Rossby waves and link weather extremes across continents, contributing thus to the synchronization of HWs in South Asia<sup>16,64</sup>.

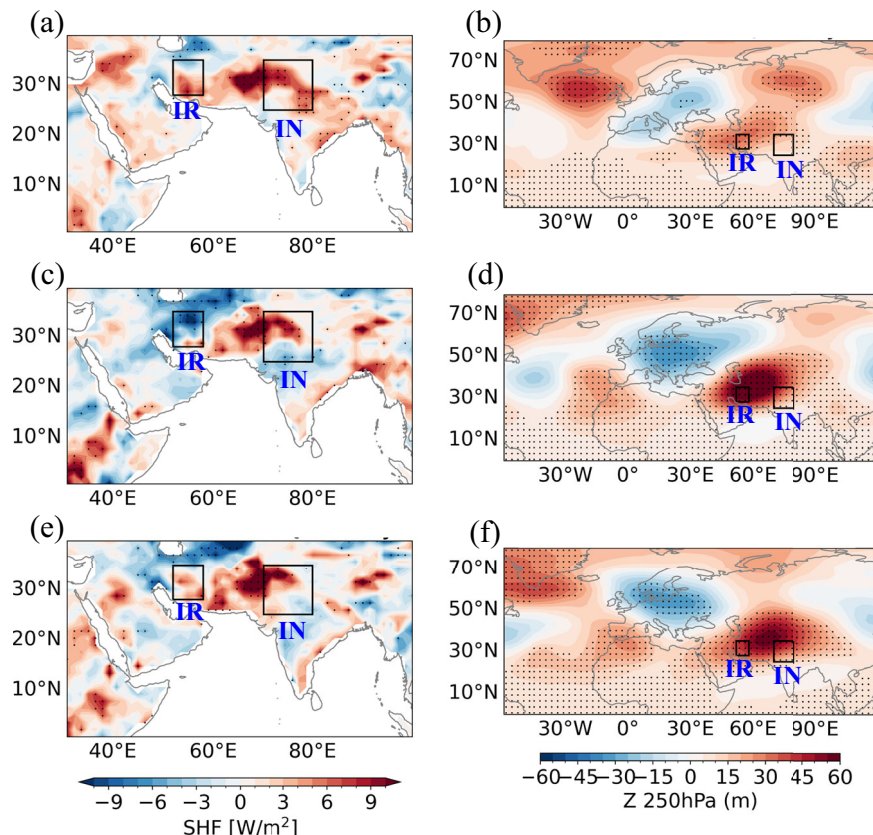
Although the regional anticyclonic conditions in the upper troposphere are similar in both historical periods, the atmospheric state over the North Atlantic associated with the synchronous HW pattern ( $HW_t \pm 5$  days) differs significantly. While in P1, a mid-upper troposphere cyclonic state is observed over the North Atlantic, in P2 the negative pressure anomalies extend to the Eurasian region (compare the rightmost columns of Figs. 6 and 7). This has been linked to the weakening of the polar jet stream<sup>21</sup>. Moreover, in P2, a significant anticyclonic flow is observed over the Greenland region, which is absent during P1. This interdecadal change in the atmospheric state over the North Atlantic sector is known to increase the variability of the Eurasian jet, as also seen from the shift in the zonal wind pattern (Uwnd) at 200 hPa over Europe and West Asia during  $HW_t$ <sup>65</sup> (refer to Fig. S7c, d in Supplementary Information).

A similar composite analysis is performed for the future climatological period based on the extreme heat network (Fig. 5) derived from model projections from CNRM-CM6-1 (Fig. 8 and Supplementary Fig. S8), MPI-ESM1.2-LR (Supplementary Figs. S9 and S10) and UKESM1-0-LL (not shown). The results reveal a high SHF anomaly pattern and local upper-tropospheric anomalous high-pressure system, similar to P2 (Fig. 8; Supplementary Figs. S9a and S10). The evolution of the SHF anomaly pattern from a few days before HW onset over IR to a few days later, when HW conditions prevail over IN, closely resemble those observed during P2 (left column in Fig. 8 and Supplementary Fig. S10), albeit with a weaker magnitude. This is likely due to the tendency of CMIP6 models underestimating SHF, as they often struggle to capture energy flux patterns associated with land cover changes and soil moisture variability, particularly over the Tibetan Plateau and arid regions like West Asia<sup>24,66,67</sup>. While a detailed SHF bias evaluation for CNRM-CM6-1 is not available and beyond the scope of this study, these general tendencies may contribute to the muted surface temperature signal in this model, as is evident from the low number of HW events and network degree. In contrast, the strong biases in turbulent heat fluxes within MPI-ESM1.2-LR do not significantly impact the surface temperature response, as the opposing biases in latent heat flux and SHF partially offset each other<sup>68</sup>.

Furthermore, a wave train associated with synchronous future projected HWs over Iran and South Asia is also observed in the upper-level meridional wind (V250) anomaly patterns (Supplementary Figs. S8 and S9b). Although the local circulation pattern in the future period is consistent among models with that of P2, the remote factors, the influence of remote drivers, particularly the atmospheric state over the North Atlantic-Greenland sector, remains uncertain. An anomalous European low, along with anomalous anticyclonic circulation over the North Atlantic-Greenland sector can be seen in the network-derived Z250 composites of both CNRM-CM6-1 and MPI-ESM1.2-LR, resembling the pattern observed in P2 (right

**Fig. 8 | Composites of daily anomalies of sensible heat flux (SHF; left column) and geopotential height at 250 hPa (Z250; right column) for the climatological period 2020–2049 under the SSP2-4.5 scenario from the CNRM-CM6-1 model.**

Composites are based on days of high extreme heat synchronization ( $HW_t$ ) between Iran (IR) and northwest India-Pakistan (IN) regions during the MAM season. Anomalies are displayed using color shading, and rectangular black boxes highlight the synchronized regions. Panels show composite anomalies for **a, b** 5 days before  $HW_t$ , **c, d** during  $HW_t$ , and **e, f** 5 days after  $HW_t$ . Black dots indicate statistically significant anomalies at the 95<sup>th</sup> percentile level.



column of Fig. 8 and Supplementary Fig. S9a). However, the high over the Greenland region is not statistically significant in MPI-ESM1.2LR projections, unlike CNRM-CM6-1. This discrepancy likely reflects broader CMIP6 uncertainties in simulating jet stream responses to future warming scenarios and model-specific differences in representing North Atlantic dynamics<sup>65,69</sup>.

Therefore, from the network-based composite analysis, we identified changes in possible local and remote factors of synchronous HWs in South Asia that occurred over the recent decades. Changes in local factors include a shift in the post-1990 period to SHF being the dominant driver of heat exchange between land and atmosphere over South Asia, which enhances diabatic warming, thereby increasing not only surface temperature but also modulating local high-pressure anomalies. The increased synchronization of South Asian HWs to West Asia, particularly Iran, during P2 suggests a change in large-scale circulation patterns. These include the role of CGT and dynamical changes over the North Atlantic-Greenland sector as identified above. In the following, we evaluate whether the causal relationships among these plausible actors have indeed undergone a transformation in recent decades.

### Changes in causal mediators of South Asian temperature variability

In order to understand the intricate interplay of the factors identified through the network-based composite analysis, that drive the spatio-temporal coherence and evolution of South Asian HWs from P1 to P2, we employ the causal network analysis<sup>70</sup> (see Causal network analysis in “Methods”). To resolve causal directionality, while avoiding the multiple testing problem, we study the intraseasonal interactions among the factors at a weekly time resolution. Thus, the time series representing the nodes are resampled to 7-day averages before the calculation of standardized anomaly. The nodes of the causal network consist of anomalous MAM temperatures over Iran ( $T_{IR}$ , averaged over IR region), anomalous MAM temperature averaged over northwest India and Pakistan ( $T_{IN}$ , averaged over IN region),

CGT index derived from Z200 anomaly of the area 35°–40°N and 60°–70°E following<sup>16,71</sup>, and North Atlantic atmospheric state represented by Z200 anomaly averaged over 33°–60°N and 75°W–25°E.

From the results of this causal network analysis shown in Fig. 9, we uncover that the mutual relationship between regional temperatures over Iran ( $T_{IR}$ ) and northwest India-Pakistan ( $T_{IN}$ ) has evolved from P1 to P2. During P1, the influence of  $T_{IR}$  on  $T_{IN}$  existed but was relatively weak (MCI = 0.122) and sporadic, with longer-lag effects suggesting slower adjustment timescales (MC1 = 0.251 at lag –1 week and –0.163 at lag –2 weeks). In contrast, during P2, not only does the instantaneous influence of  $T_{IR}$  on  $T_{IN}$  become stronger and more significant (MCI = 0.209), but also the positive lagged influence at –1 week has increased. This aligns well with our partial degree analysis (Fig. 4), indicating that hot extremes in these adjacent regions are increasingly co-occurring, consistent with recent findings on compound HW dynamics across South Asia and the Middle East. This shift likely reflects intensified regional land-atmosphere interactions due to enhanced surface warming, reduced soil moisture, and stronger thermal gradients under recent climate change as discussed in the previous section<sup>72</sup>.

$T_{IR}$ ,  $T_{IN}$ , and CGT have an instantaneous (within a week) triangular relationship with each other in both periods. This relationship is due to the presence of the common persistent mid-to-upper tropospheric anticyclone over the area (Figs. 6d, h, l and 7d, h, l). The lagged causal relationship  $T_{IR} \rightarrow T_{IN}$  discussed earlier at lag –1 to –2 weeks may signify the eastward propagation of a high-pressure system towards India along the subtropical jet via CGT. The positive causal relationship from  $T_{IR}$ (–1 week) → CGT has strengthened in the later period (MCI = 0.178 in P1 whereas 0.314 during P2). The feedback from regional temperatures ( $T_{IR}$  and  $T_{IN}$ ) to CGT has become stronger and more temporally consistent since post-1990. This indicates enhanced land-atmosphere coupling likely due to the abnormal land surface warming over West Asia in the recent decades during spring, which triggers anomalous Rossby waves by diabatic heating downstream, facilitating the intensification of early summer CGT<sup>18,73</sup>. The strengthening of the instantaneous CGT –  $T_{IN}$  relationship in P2 aligns with the increased

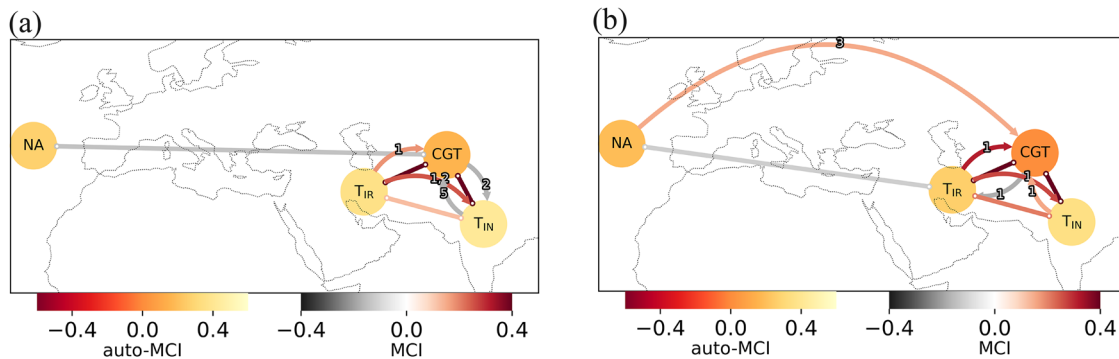


**Fig. 9 | Causal effect networks of identified factors influencing South Asian MAM temperature anomalies during two historical periods.** Causal effect networks are shown for **a** 1960–1989 and **b** 1990–2019. The nodes of the network represent identified atmospheric subprocesses and are denoted by colored circles. Directed links between nodes indicate statistically significant causal influences, with colors

representing the strength of the influence (measured by Momentary Conditional Independence, MCI). Numbers on the links denote the time lag in weeks. Node colors reflect the strength of self-influence (auto-MCI), while link colors denote the magnitude of causal impact between subprocesses.

influence of springtime CGT in facilitating April–May extreme heat events over the southern Tibetan Plateau<sup>74</sup>. This is consistent with our network analysis, which showed an increase in HW connectivity over this region (Figs. 2b and 4b,d). Additionally, several longer-lagged causal links present in the earlier period (e.g.,  $T_{IN}$  (−5 weeks) → CGT, CGT (−2 weeks) →  $T_{IN}$ ) are absent in the later period, suggesting a shortening of feedback timescales. Interestingly, CGT also has a weak negative influence on  $T_{IR}$  during P2, which was absent during P1.

Besides the complex interrelationship among CGT and regional anomalous temperatures over West and South Asia, the influence of the North Atlantic (NA) atmospheric state on this region has also undergone notable changes. The significant instantaneous relationship between the CGT and NA in P1, disappears in P2. On the other hand, a new causal link between regional temperature anomalies of Iran ( $T_{IR}$ ) and NA emerges in P2. Furthermore, a new lagged positive influence (MCI = 0.153) from NA at lag −3 weeks to CGT appears in P2, potentially indicating a delayed downstream response of CGT to Atlantic sector dynamics<sup>71</sup>. This may be associated with altered jet stream or waveguide pathways in recent decades, consistent with recent findings that highlight the increasing influence of North Atlantic variability on the Eurasian westerly jet<sup>65</sup>. Tables S1 and S2 in the Supplementary Information summarize the quantitative differences in causal relationships among the key variables between P1 and P2.

Although the causal analysis employed here is based on anomalous climate time series, it is assumed that the mechanisms that drive anomalies over a multi-day period will contribute to or exacerbate extreme heat conditions, as the HW events will typically be embedded within periods of sustained high anomalies. Furthermore, by analyzing 7-day averages, we capture the persistent atmospheric or climatic conditions that contribute to extreme events. Hence, our findings from the causal network analysis validate the observed changes in HW synchronization patterns over South Asia, reinforcing the changes in land-atmospheric processes identified through the network-derived composite analysis. They further highlight the evolving influence of large-scale circulation patterns in driving synchronized heat events across the region.

We restrict the causal network analysis to the historical periods only because, as discussed earlier, the uncertainties in the representation of atmospheric circulation, particularly over the North Atlantic–Greenland sector in CMIP6 models, make it difficult to draw reliable causal inferences about future HW patterns<sup>75,76</sup>. Addressing these discrepancies would require a more comprehensive, model-specific assessment of CMIP6 circulation responses, which is beyond the scope of this study.

## Discussions

In this paper, we explored changes in the spatiotemporal coherence pattern of South Asian heatwaves (HWs) over two historical (1960–1989 and

1990–2019) and one future 30-year climatological periods (2020–2049). Our findings highlight significant changes in the processes driving synchronous patterns of South Asian HWs over these decades and their broader climatic impacts as discussed below. The event synchronization-based complex network analysis revealed that there is a substantial increase in synchronous spring HW events between northwest India and Pakistan region and Iran in the later historical climatological period. An overall eastward shift of the region with the strongest spatial synchronization from West Asia (before 1990) to Pakistan, northwest India, and the southwestern Tibetan Plateau region by mid 21st century is projected under a realistic warming scenario.

This increasing node centrality in South Asia post-1990 warming is found to be related to the enhanced surface sensible heat flux (SHF) in this region. The spatial pattern of the upward SHF anomaly obtained from the composite analysis of synchronous HW events between Iran and northern India–Pakistan regions resembles greatly the network topological structure of the region. This emphasizes the pivotal role of SHF in driving land-atmospheric feedback processes in the recent decades and in increasing diabatic heating. This not only increases surface temperatures but also contributes to the strengthening of local anticyclonic conditions over West and South Asia. Therefore, the anomalous upward SHF forms the backbone of the extreme temperature climate network, reflecting the heat vulnerability of the region which could be important for a heat risk assessment.

Additionally, the study reveals a change in the influence of atmospheric conditions over the North Atlantic–Greenland sector on the synchronization pattern of South Asian HWs in the later climatological period. The altered atmospheric state of the North Atlantic is found to have an increased positive causal influence on the early-summer circumglobal teleconnection (CGT). Furthermore, the feedback from regional temperatures in West and South Asia to CGT has also strengthened post-1990, as revealed by the network-derived composite and causal analysis. This anomalous strengthening of the early-summer CGT in recent decades is primarily driven by a significant increase in spring diabatic heating (enhanced SHF) over West and South Asia, coupled with dynamic changes in the North Atlantic–Greenland sector. Although it is well established that CGT plays a key role in influencing the Asian monsoon and heat extremes in East Asia during June–July–August<sup>18,64,77</sup>, its modulation of spring anomalous temperature over South Asia due to its earlier intensification, is an important finding.

In light of recent studies showing a trend of depletion of soil moisture in South Asia due to global warming<sup>77</sup>, our findings on the central role of SHF in driving synchronous patterns of South Asian HWs in recent decades as well as in future projections, clearly indicate an increasing sensitivity of the atmosphere to land surface drying. Studies have shown that although forecast models struggle to represent the soil moisture feedback regime, their performance in predicting extreme heat events is more effective in the

hypersensitive regime, when soil moisture is sufficiently low, such that SHF becomes the dominant driver of energy transfer from the land to the atmosphere<sup>78</sup>. This potentially explains the high predictability of the 2022 spring HWs in northwest India and Pakistan<sup>28</sup>. A detailed temperature budget analysis, which can provide further quantitative insights into the thermodynamic processes underlying heatwave formation in South Asia, is an important direction for future research to complement the broader patterns presented in this study.

This study not only uncovers persistent local and remote atmospheric conditions in the recent period, which can enhance the HW forecast skill, but also provides valuable information to understand HW predictability in subseasonal to seasonal time forecasts. These findings highlight the critical need for high-quality observations of energy and water fluxes in the soil and at the land surface, particularly in regions such as South Asia, which are undergoing significant land use and land cover changes. Such observations are essential for advancing our process understanding of land-atmosphere feedbacks and improving parameterizations of surface fluxes in models. These improvements will enhance prediction in regions where land cover changes may amplify climate feedbacks, having significant implications for heat risk assessment and climate resilience planning in a warming world.

Our reanalysis-based findings on the enhanced influence of the North Atlantic atmospheric state on South Asian HWs via West Asia and the CGT highlight the need for a rigorous model-based analysis, taking into account model differences in heat fluxes, North Atlantic SST variability, air-sea coupling strength, internal variability, and the representation of remote teleconnections. Given the uncertainties in the representation of the North Atlantic circulation in CMIP6 models<sup>75,79</sup>, a future direction of this work would be to focus on assessing projections of these critical interactions under changing climates and their impacts on climate extremes.

## Methods

### Data

We divide our period of analyses into two historical and one future 30-year periods to compare the spatiotemporal patterns of extreme heat conditions in these periods, namely, 1960–1989 (P1), 1990–2019 (P2) and 2020–2049. For the historical periods, we use the daily 2m-temperature (T2m) data from ERA5 at the spatial resolution of  $1^\circ \times 1^\circ$  for the time period 1960–2019<sup>80</sup>. Furthermore, we employ results from the CMIP6 concentration-driven simulations of the projected evolution of the 2m-temperature (tas) for the period 2020–2049 by the MPI-Earth System model, CNRM-CM6 and UKESM. The model configuration MPI-ESM1.2-LR<sup>81</sup> used here has a coarser spatial resolution of  $\sim 200$  km. We used the mean projected T2m of the 10-member ensemble simulations for the more realistic scenario SSP2-4.5 (Shared Socioeconomic Pathways) with an additional radiative forcing of  $4.5 \text{ W/m}^2$  by the year 2100 representing the medium pathway of future greenhouse gas emissions given current policies and assuming modest climate protection measures are being taken<sup>82</sup>. Additionally, for the model CNRM-CM6-1, we use the ensemble mean of the 5-member simulations for the SSP2-4.5 scenario<sup>83</sup>. This model configuration has model horizontal resolution is about  $1.4^\circ$  at the equator ( $\sim 155$  km). Similarly, the ensemble mean of the 6-member simulations for the same forcing scenario from the UKESM1-0-LL model is used, which has a spatial resolution of  $1.25^\circ \times 1.875^\circ$ <sup>84</sup>. Using the SSP2-4.5 scenario allows us to make more plausible future projections of the spatiotemporal connectivity pattern of extreme heat events as opposed to projecting SSP5-8.5, which represents the worst-case scenario<sup>85</sup>.

We investigate the interdecadal changes of HWs covariability patterns across tropical and subtropical regions of South-Central and West Asia ( $0^\circ\text{--}40^\circ\text{N}$  and  $30^\circ\text{E}\text{--}100^\circ\text{E}$ ), with a particular emphasis on the HWs occurring in the Indian subcontinent ( $5^\circ\text{N}\text{--}40^\circ\text{N}$  and  $70^\circ\text{E}\text{--}100^\circ\text{E}$ ). As we are interested in continental HWs, we limit our analysis to grid points on land only. Moreover, we primarily focus on the extreme heat events occurring during the pre-monsoon period (March-April-May, MAM), when the region normally experiences a strong diabatic heating, which facilitates the onset of the Indian Summer Monsoon in June.

In order to unravel the atmospheric circulations modulating the temperature conditions over the area under study, we use geopotential height (Z), zonal (Uwind) and meridional (Vwind) components of wind, sensible heat flux (SHF), and outgoing longwave radiation (OLR) from the corresponding datasets of the different periods at the same spatial and temporal resolution as for temperature. The convention for SHF is positive upwards (from the land into the atmosphere). OLR is derived by reversing the sign of the ERA5 variable mean top net long-wave radiation flux, as the ERA5 convention for vertical fluxes is positive downwards.

### Heatwave identification

While several definitions to identify a HW event exist in literature<sup>27,86</sup>, we define an event as a HW when the daily T2m anomaly exceeds one standard deviation and persists for at least five consecutive days, following<sup>14</sup>. This definition provides a climate-sensitive and adaptive approach that captures both variations in frequency and intensity across different regions. Unlike fixed percentile-based definitions<sup>87,88</sup>, which impose a uniform number of HW events at all locations, this method accounts for local climate variability<sup>89,90</sup>, allowing the HW frequency to naturally vary according to regional warming trends. The temperature anomaly for a study period (e.g., 1960–1989) is computed by subtracting the climatology of that respective period. We compute the HWs index for all the grid points according to the definition above. When a HW event spans multiple days (e.g., a five-day sequence), it is treated as a single event rather than multiple daily events. For applications involving the complex network method, we assign the event to the first day of the sequence, which serves as the representative timestamp for that event.

Further details on the robustness of this definition, including comparisons with percentile-based method, are provided under the subheading 'Robustness tests' below.

### Functional network construction using event synchronization

The constructed HW time series belongs to the category of event-like data, characterized by irregular sampling<sup>91</sup>. In order to obtain an objective and comparable estimate of the synchronization between two event series at varying time scales, we use event synchronization (ES), as conventional similarity measures such as linear correlation are unsuitable due to their non-Gaussian nature<sup>31</sup>. The measure is preferable in applications to real-world data for which there is no validated knowledge about the relevant time scales, as it is time-scale adaptive within a range of allowed time delays. In case of climate applications, the dynamic choice of delay enables the method to take into account a potentially changing density of events, due to varying scales of the driving atmospheric processes. Owing to its advantages, ES has been successfully used to unravel the covariability patterns of different climate extremes, such as extreme rainfall, heatwaves, typhoons, droughts, etc.<sup>32,33,35,37,39,92</sup>.

Here, our study employs an improved version of ES, proposed in<sup>32</sup>, in our study which is defined as follows: Consider two event series  $\{Tx_i^\mu\}_{\mu=1,\dots,l_i}$  and  $\{Tx_j^\nu\}_{\nu=1,\dots,l_j}$ , where  $l_i$  and  $l_j$  are events corresponding to the grid points  $i$  and  $j$ ,  $\{Tx_i^\mu\}$  denotes the  $\mu$ th event at the grid point  $i$ . The waiting time between two events  $\{Tx_i^\mu\}, \{Tx_j^\nu\}$  is computed as  $t_{i,j}^{\mu,\nu} = \|Tx_i^\mu - Tx_j^\nu\|$ . We say events  $Tx_i^\mu$  and  $Tx_j^\nu$  are synchronous if  $t_{i,j}^{\mu,\nu} \leq \tau_{i,j}^{\mu,\nu}$  where  $\tau_{i,j}^{\mu,\nu} = \frac{\min(t_{i,i}^{\mu,\mu-1}, t_{i,i}^{\mu+1,\mu}, t_{j,j}^{\nu,\nu-1}, t_{j,j}^{\nu+1,\nu})}{2}$ . A maximum temporal delay  $\tau_{\max}$  is used to avoid unreasonably high delays between events at different locations. Now, we define ES for each pair of nodes  $(i, j)$  as

$$\text{ES}_{ij} = |\{(\mu, \nu) : t_{i,j}^{\mu,\nu} \leq \min(\tau_{i,j}^{\mu,\nu}, \tau_{\max})\}| \quad (1)$$

where  $|S|$  denotes the cardinality of the set  $S$ .

The geographical grid points of the climate dataset are considered as the  $N$  nodes of the functional climate network. We construct the climate network by measuring the interrelations between the event series using ES for all pairwise combinations of grid points  $i$  and  $j$ , where  $i, j \in N$ . The

statistical significance of each empirical value is determined on the basis of a null model distribution. This is numerically obtained by computing ES for a large number of pairs of surrogate event series with  $l_i$  and  $l_j$  number of events distributed uniformly and randomly within the season under consideration (here, March-April-May). For each pair  $(l_i, l_j)$  of event numbers, the 99<sup>th</sup> percentile of the corresponding distribution is determined as the significance threshold. Finally, a network link is placed between grids  $i$  and  $j$  if  $ES_{ij}^{\mu}$  is significantly above this threshold at a significance level of 0.01. Consequently, the corresponding element in the network adjacency matrix is set to  $A_{ij} = 1$  if the link is present, and  $A_{ij} = 0$  otherwise. This approach ensures that potential biases due to increased event counts are effectively excluded through the use of this statistical threshold.

## Network measures

Quantifying the network topology using various network measures provides insights into the underlying dynamics of the system across different spatial scales<sup>93</sup>. We employ the node-based network centrality measure *degree*  $k_i$ , which quantifies the number of connections a node  $i$  has with all other nodes in the network:

$$k_i = \sum_{j=1}^N A_{ij} \quad (2)$$

Regions with high-degree values represent areas with strong spatial connectivity, implying that variability at those locations is strongly linked to multiple other regions. In the particular context of HW networks, the degree of a node provides information about the number of grid points where synchronous HWs occur. In the case of extreme events, such as heatwaves or extreme precipitation, high-degree regions are particularly important because they often reflect the influence of large-scale atmospheric circulation patterns that drive coherent extremes over extended areas<sup>94–96</sup>. Conversely, low-degree regions typically indicate localized or isolated variability<sup>97</sup>, often governed by small-scale processes or topographic constraints, and may correspond to regions where extreme events are less spatially coherent.

To gain further insight into the connectivity of a specific region of interest  $R$ , we also calculate the partial degree of the nodes in the network connected to the region  $R$ . The partial degree, denoted as  $k_i^R$ , yields the number of links connecting a node  $i$  with the nodes  $j \in R$ , i.e.,

$$k_i^R = \sum_{j \in R} A_{ij} \quad (3)$$

This measure helps to decompose the total degree spatially, indicating how strongly each node is connected to the region  $R$  (Fig. 4). Importantly, if we sum the partial degrees from all nodes in the network to region  $R$ , we obtain the total degree of region  $R$  using equations (2) and (3):

$$\sum_{i=1}^N k_i^R = \sum_{i=1}^N \sum_{j \in R} A_{ij} = \sum_{j \in R} \sum_{i=1}^N A_{ij} = \sum_{j \in R} k_j \quad (4)$$

This identity ensures consistency between the spatial distribution of links (as shown in partial degree plots in Fig. 4) and the overall network structure (Fig. 3). It should be noted that the partial degree is proportional to the number of nodes in the target region  $R$ . The approach is analogous to one-point correlation maps of climate variables, but identifies regions with similar underlying dynamics leading to synchronous extreme events<sup>39</sup>.

## Identification of synchronization days for composite analysis

The aforementioned definition of ES in equation (1) can be modified to detect days when strong synchronization of extreme events occurs between two spatially distributed regions while maintaining the temporal ordering of events. Each region comprises multiple grid points, with each grid point

associated with heatwave (HW) event series, based on the definition introduced earlier. Let  $R_1$  and  $R_2$  denote the sets of HW time series corresponding to regions *IR* ( $28^\circ\text{--}35^\circ\text{N}$ ,  $52^\circ\text{--}58^\circ\text{E}$ ) and *IN* ( $25^\circ\text{--}35^\circ\text{N}$ ,  $70^\circ\text{--}80^\circ\text{E}$ ), respectively. We then form the Cartesian product  $R_1 \times R_2$ , which consists of all possible pairs of grid points  $(i, j)$  such that  $i \in R_1$  and  $j \in R_2$ . For each such pair, we evaluate whether a HW event at grid point  $i$  in region *IR* is followed by a HW event at grid point  $j$  in region *IN* within a specified time lag  $\tau_{\max}$ . Formally, we compute

$$ES_{R_1 \rightarrow R_2}^{\mu} := |\{(i, j) \in R_1 \times R_2 : -\tau_{i,j}^{\mu,v} < t_{i,j}^{\mu,v} \leq 0 \wedge |t_{i,j}^{\mu,v}| \leq \tau_{\max}\}| \quad (5)$$

Thus,  $ES_{R_1 \rightarrow R_2}^{\mu}$  gives us a daily time series denoting the number of events in the region  $R_1$  that have a uniquely associative subsequent event in the region  $R_2$  within the maximum allowed temporal delay  $\tau_{\max}$ . We then determine the specific synchronization days as any day for which  $ES_{R_1 \rightarrow R_2}^{\mu} > 0$ , indicating that at least one grid-point pair across the regions exhibits a temporally ordered HW event within the allowed time lag. The daily time series of  $ES_{R_1 \rightarrow R_2}^{\mu}$  provides a quantitative measure of how strongly the two regions are synchronized on each day.

Finally, we use the days identified by nonzero values of  $ES_{R_1 \rightarrow R_2}^{\mu}$  (denoted as *HW<sub>t</sub>*) to compute composite anomalies of relevant climate variables—such as geopotential height, wind, temperature sensible heat flux, and outgoing longwave radiation—associated with synchronized extreme heat events between regions *IR* and *IN*.

This approach allows us to isolate instances of coherent, temporally linked heat extremes, which may be influenced by shared or teleconnected atmospheric conditions<sup>32,39</sup>.

## Causal network analysis

We employed the Peter and Clark Momentary Conditional Independence (PCMCI) algorithm to infer causal relationships from observational time series<sup>98,99</sup>. Unlike simple correlation or classical Granger causality, which can be affected by confounding variables, PCMCI is designed to identify and remove spurious statistical associations through iterative conditioning. The algorithm proceeds in two main steps<sup>71</sup>:

**PC-step:** This initial step identifies a refined set of potential direct predictors ('parents') for each variable by systematically testing for statistically significant partial correlations while conditioning on other potential predictors. This helps filter out indirect links and reduces the set of variables considered in the next step.

**MCI-step:** The second stage, the Momentary Conditional Independence (MCI) test, estimates the strength and direction of the causal links. The algorithm calculates their partial correlation for every possible pair of 'actors' in the system. This calculation is performed by conditioning on the combined set of potential parents identified in the preceding PC-step. This rigorous conditioning on the comprehensive set of potential confounders helps to isolate the direct causal influence between the pair of variables being tested. After assessing all variable pairs, the final set of causal parents is identified for each actor. The *causal effect coefficient*, known as the MCI, is then calculated for each identified causal link. This is typically done by performing a multivariate linear regression where the target actor's time series is regressed onto the time series of its identified set of causal parents at their respective causal lags. Importantly, the MCI test assesses whether a variable  $X_{t-\tau}$  provides information about  $Y_t$  beyond what is already contained in the parents of  $Y$  and  $X$ . If it does,  $X$  is said to be a potential causal driver of  $Y$  at lag  $\tau$ .

In addition to causal links between different variables, PCMCI also identifies the time-delayed self-influence of a variable on itself. The strength of this influence is quantified by the auto-MCI ( $X_{t-\tau} \rightarrow X_t$ ). This coefficient represents how much a variable's value at a certain past time step directly affects its value at the current time step. These reflect the persistence or memory of a variable's past values on its present state.

The results of the PCMCI analysis are commonly visualized using Causal Effect Networks (CENs). In a CEN, nodes represent variables, and directed edges (arrows) indicate the direction of causality identified by the

algorithm. The color of the edges (arrows) typically represents the strength of the causal link, corresponding to the MCI, while the color of the nodes can represent the auto-MCI.

To ensure the statistical significance of the identified causal links, particularly given the numerous tests performed (especially in causal maps involving many grid points), a significance threshold ( $p$ -values = 0.05 in this study) is applied. Furthermore, to control for the increased chance of false positives from multiple comparisons, the  $p$ -values for all tests are adjusted using the Benjamini-Hochberg false discovery rate (FDR) correction<sup>100</sup>. This adjustment helps to ensure that the reported causal links are statistically robust.

### Robustness tests

Here, we show that our statistical analyses are robust to variations of the different parameter values chosen in the main text. To assess the sensitivity of our results to the HW definition, we compared our standard deviation-based approach with a percentile-based threshold (90<sup>th</sup> percentile) following<sup>88</sup>). The overall number of events is obviously lower in the 90<sup>th</sup> percentile threshold compared to the standard deviation-based selection of events, as the former captures only the most extreme values, whereas the latter typically includes more moderate deviations from the mean (Supplementary Fig. S11a, c). Despite this difference, the spatial and temporal patterns of HW occurrences-and the resulting network structures-remain broadly consistent across both methods (see Supplementary Fig.S11). This supports the robustness of our conclusions. We further tested the effect of varying the minimum duration for defining HW events. As shown in Supplementary Fig. S12, the network degree patterns remain broadly consistent with Fig. 2 even when HW events are defined as daily T2m anomalies exceeding one standard deviation for at least 7 consecutive days.

Moreover, our results are only weakly sensitive to different choices of the maximum time delay  $\tau_{\max}$  used to detect synchronized events; we find consistent outcomes for both  $\tau_{\max} = 5$  and  $\tau_{\max} = 7$  days (see Supplementary Fig. S13).

### Data availability

ERA5 data used for this study is freely available and can be downloaded from <https://cds.climate.copernicus.eu/datasets>. The CMIP6 simulation outputs used in this study is also freely available for download via <https://esgf-data.dkrz.de/search/cmip6-dkrz/>. The underlying code for this study is not publicly available, but may be made available to qualified researchers on reasonable request from A.B. and S.G.

Received: 20 March 2025; Accepted: 20 June 2025;

Published online: 05 August 2025

### References

- Shaw, R. et al. in *Climate Change 2022: Impacts, Adaptation and Vulnerability. Contribution of Working Group II to the Sixth Assessment Report of the Intergovernmental Panel on Climate Change* (eds Pörtner, H.-O. et al.) 1457–1579 (Cambridge University Press, 2022).
- Intergovernmental Panel on Climate Change. *IPCC AR6 WGI Regional Fact Sheet—Asia*. [https://www.ipcc.ch/report/ar6/wg1/downloads/factsheets/IPCC\\_AR6\\_WGI\\_Regional\\_Fact\\_Sheet\\_Asia.pdf](https://www.ipcc.ch/report/ar6/wg1/downloads/factsheets/IPCC_AR6_WGI_Regional_Fact_Sheet_Asia.pdf) (IPCC, 2021).
- India Meteorological Department. *FAQ\_heat\_wave.pdf*. [https://internal.imd.gov.in/pages/heatwave\\_mausam.php](https://internal.imd.gov.in/pages/heatwave_mausam.php) (India Meteorological Department, 2024).
- Zhao, Q. et al. Global, regional, and national burden of mortality associated with non-optimal ambient temperatures from 2000 to 2019: a three-stage modelling study. *Lancet Planet. Health* **5**, e415–e425 (2021).
- World Health Organization. *Climate Change, Heat and Health*, accessed 6 September 2024. <https://www.who.int/news-room/fact-sheets/detail/climate-change-heat-and-health> (WHO, 2023).
- Zhao, C. et al. Temperature increase reduces global yields of major crops in four independent estimates. *Proc. Natl. Acad. Sci. USA* **114**, 9326–9331 (2017).
- Lesk, C. et al. Compound heat and moisture extreme impacts on global crop yields under climate change. *Nat. Rev. Earth Environ.* **3**, 872–889 (2022).
- Kemter, M. et al. Cascading hazards in the aftermath of Australia’s 2019/2020 Black Summer wildfires. *Earth’s Future* **9**, e2020EF001884 (2021).
- World Meteorological Organization. *Climate Change Made Heatwaves in India and Pakistan “30 Times More Likely”*. <https://wmo.int/media/news/climate-change-made-heatwaves-india-and-pakistan-30-times-more-likely> (World Meteorological Organization, 2022).
- Wang, C. et al. Drought-heatwave compound events are stronger in drylands. *Weather Clim. Extremes* **42**, 100632 (2023).
- Tripathy, K. P., Mukherjee, S., Mishra, A. K., Mann, M. E. & Williams, A. P. Climate change will accelerate the high-end risk of compound drought and heatwave events. *Proc. Natl. Acad. Sci.* **120**, e2219825120 (2023).
- Sauter, C., Catto, J. L., Fowler, H. J., Westra, S. & White, C. J. Compounding heatwave-extreme rainfall events driven by fronts, high moisture, and atmospheric instability. *J. Geophys. Res. Atmos.* **128**, e2023JD038761 (2023).
- Zscheischler, J. et al. Future climate risk from compound events. *Nat. Clim. Change* **8**, 469–477 (2018).
- Ratnam, J., Behera, S. K., Ratna, S. B., Rajeevan, M. & Yamagata, T. Anatomy of Indian heatwaves. *Sci. Rep.* **6**, 1–11 (2016).
- Ganeshi, N. G., Mujumdar, M., Krishnan, R. & Goswami, M. Understanding the linkage between soil moisture variability and temperature extremes over the Indian region. *J. Hydrol.* **589**, 125183 (2020).
- Ding, Q. & Wang, B. Circumglobal teleconnection in the Northern Hemisphere summer. *J. Clim.* **18**, 3483–3505 (2005).
- Kornhuber, K. et al. Amplified Rossby waves enhance risk of concurrent heatwaves in major breadbasket regions. *Nat. Clim. Change* **10**, 1–6 (2020).
- Yang, J. et al. Atmospheric circumglobal teleconnection triggered by spring land thermal anomalies over West Asia and its possible impacts on early summer climate over northern China. *J. Clim.* **34**, 5999–6021 (2021).
- Rohini, P., Rajeevan, M. & Srivastava, A. On the variability and increasing trends of heat waves over India. *Sci. Rep.* **6**, 1–9 (2016).
- Vittal, H., Villarini, G. & Zhang, W. On the role of the Atlantic Ocean in exacerbating Indian heat waves. *Clim. Dyn.* **54**, 1887–1896 (2020).
- Dubey, A. K., Kumar, P., Saharwardi, M. S. & Javed, A. Understanding the hot season dynamics and variability across India. *Weather Clim. Extrem.* **32**, 100317 (2021).
- Jha, R., Mondal, A., Ghosh, S. & Murtugudde, R. Northward shift of pre-monsoon zonal winds exacerbating heatwaves over India. *Geophys. Res. Lett.* **51**, e2024GL110486 (2024).
- Pai, D., NAIR, S. & Ramanathan, A. Long term climatology and trends of heat waves over India during the recent 50 years (1961–2010). *Mausam* **64**, 585–604 (2013).
- Rohini, P., Rajeevan, M. & Mukhopadhyay, P. Future projections of heat waves over India from CMIP5 models. *Clim. Dyn.* **53**, 975–988 (2019).
- Singh, S., Mall, R. & Singh, N. Changing spatio-temporal trends of heat wave and severe heat wave events over India: An emerging health hazard. *Int. J. Climatol.* **41**, E1831–E1845 (2021).
- Zhang, W., Xu, Z. & Guo, W. Investigating the relative contribution of anthropogenic increase in greenhouse gas and land use and land cover change to Asian climate: a dynamical downscaling study. *Int. J. Climatol.* **42**, 9656–9675 (2022).

27. Barriopedro, D., García-Herrera, R., Ordóñez, C., Miralles, D. & Salcedo-Sanz, S. Heat waves: physical understanding and scientific challenges. *Rev. Geophys.* **61**, e2022RG000780 (2023).
28. European Centre for Medium-Range Weather Forecasts. *Spring Heatwave in India and Pakistan*, accessed 6 September 2024. <https://www.ecmwf.int/en/newsletter/172/news/spring-heatwave-india-and-pakistan>(European Centre for Medium-Range Weather Forecasts, 2022).
29. Hannachi, A., Jolliffe, I. T. & Stephenson, D. B. Empirical orthogonal functions and related techniques in atmospheric science: a review. *Int. J. Climatol.* **27**, 1119–1152 (2007).
30. Fan, J. et al. Statistical physics approaches to the complex Earth system. *Phys. Rep.* **896**, 1–84 (2021).
31. Quiroga, R. Q., Kreuz, T. & Grassberger, P. Event synchronization: a simple and fast method to measure synchronicity and time delay patterns. *Phys. Rev. E* **66**, 041904 (2002).
32. Boers, N. et al. Complex networks reveal global pattern of extreme rainfall teleconnections. *Nature* **566**, 373–377 (2019).
33. Malik, N., Bookhagen, B., Marwan, N. & Kurths, J. Analysis of spatial and temporal extreme monsoonal rainfall over South Asia using complex networks. *Clim. Dyn.* **39**, 971–987 (2012).
34. Agarwal, A., Guntu, R. K., Banerjee, A., Gadhawale, M. A. & Marwan, N. A complex network approach to study the extreme precipitation patterns in a river basin. *Chaos Interdiscip. J. Nonlinear Sci.* **32**, 013113(2022).
35. Mondal, S. & Mishra, A. K. Complex networks reveal heatwave patterns and propagations over the USA. *Geophys. Res. Lett.* **48**, e2020GL090411 (2021).
36. Dar, J. A. & Apurv, T. Spatiotemporal characteristics and physical drivers of heatwaves in India. *Geophys. Res. Lett.* **51**, e2024GL109785 (2024).
37. Konapala, G. & Mishra, A. Review of complex networks application in hydroclimatic extremes with an implementation to characterize spatio-temporal drought propagation in continental USA. *J. Hydrol.* **555**, 600–620 (2017).
38. Giaquinto, D., Marzocchi, W. & Kurths, J. Exploring meteorological droughts' spatial patterns across Europe through complex network theory. *Nonlinear Process. Geophys.* **30**, 167–181 (2023).
39. Gupta, S. et al. Interconnection between the Indian and the East Asian summer monsoon: spatial synchronization patterns of extreme rainfall events. *Int. J. Climatol.* **43**, 1034–1049 (2023).
40. Choi, N., Lee, M.-I., Cha, D.-H., Lim, Y.-K. & Kim, K.-M. Decadal changes in the interannual variability of heat waves in East Asia caused by atmospheric teleconnection changes. *J. Clim.* **33**, 1505–1522 (2020).
41. Samset, B. H. et al. Steady global surface warming from 1973 to 2022 but increased warming rate after 1990. *Commun. Earth Environ.* **4**, 400 (2023).
42. World Meteorological Organization. *State of the Climate in Asia 2022*.<https://library.wmo.int/idurl/4/66314>(WMO, 2023).
43. Turner, A. G. & Annamalai, H. Climate change and the South Asian summer monsoon. *Nat. Clim. Change* **2**, 587–595 (2012).
44. De Sherbinin, A., Schiller, A. & Pulsipher, A., The vulnerability of global cities to climate hazards. *Environ. Urban.* **19**, 39–64 (2007).
45. Pfahl, S. & Wernli, H. Quantifying the relevance of atmospheric blocking for co-located temperature extremes in the Northern Hemisphere on (sub-) daily time scales. *Geophys. Res. Lett.* **39**, L12807 (2012).
46. Röhlisberger, M. & Papritz, L. Quantifying the physical processes leading to atmospheric hot extremes at a global scale. *Nat. Geosci.* **16**, 210–216 (2023).
47. Perkins, S. E., Alexander, L. & Nairn, J. Increasing frequency, intensity and duration of observed global heatwaves and warm spells. *Geophys. Res. Lett.* **39**, L20714 (2012).
48. Perkins-Kirkpatrick, S. & Lewis, S. Increasing trends in regional heatwaves. *Nat. Commun.* **11**, 3357 (2020).
49. Russo, S., Sillmann, J. & Fischer, E. M. Top ten European heatwaves since 1950 and their occurrence in the coming decades. *Environ. Res. Lett.* **10**, 124003 (2015).
50. Dalal, G., Pathania, T., Koppa, A. & Hari, V. Drivers and mechanisms of heatwaves in South West India. *Clim. Dyn.* **62**, 5527–5541 (2024).
51. Neupane, S., Shrestha, S., Ghimire, U., Mohanasundaram, S. & Ninsawat, S. Evaluation of the CORDEX regional climate models (RCMs) for simulating climate extremes in the Asian cities. *Sci. Total Environ.* **797**, 149137 (2021).
52. Singh, S., Mall, R., Singh, P. K., Bhatla, R. & Choubey, P. K. How virtuous are the bias corrected CMIP6 models in the simulation of heatwave over different meteorological subdivisions of India? *Urban Clim.* **55**, 101936 (2024).
53. Norgate, M., Tiwari, P., Das, S. & Kumar, D. On the heat waves over India and their future projections under different SSP scenarios from CMIP6 models. *Int. J. Climatol.* **44**, 973–995 (2024).
54. Lalande, M., Ménégoz, M., Krinner, G., Naegeli, K. & Wunderle, S. Climate change in the High Mountain Asia in CMIP6. *Earth Syst. Dyn.* **12**, 1061–1098 (2021).
55. Perkins, S. E. A review on the scientific understanding of heatwaves –their measurement, driving mechanisms, and changes at the global scale. *Atmos. Res.* **164**, 242–267 (2015).
56. Li, X. et al. Role of atmospheric resonance and land-atmosphere feedbacks as a precursor to the June 2021 Pacific Northwest Heat Dome event. *Proc. Natl. Acad. Sci. USA* **121**, e2315330121 (2024).
57. Zhang, K. et al. A global dataset of terrestrial evapotranspiration and soil moisture dynamics from 1982 to 2020. *Sci. Data* **11**, 445 (2024).
58. Liu, W., Shi, N., Wang, H. & Huang, Q. Thermodynamic characteristics of extreme heat waves over the middle and lower reaches of the Yangtze River Basin. *Clim. Dyn.* **62**, 3877–3889 (2024).
59. Dirmeyer, P. A. The terrestrial segment of soil moisture-climate coupling. *Geophys. Res. Lett.* **38**, L16702 (2011).
60. Ha, K.-J. et al. Dynamics and characteristics of dry and moist heatwaves over East Asia. *npj Clim. Atmos. Sci.* **5**, 49 (2022).
61. Fischer, E. M., Seneviratne, S. I., Vidale, P. L., Lüthi, D. & Schär, C. Soil moisture–atmosphere interactions during the 2003 European summer heat wave. *J. Clim.* **20**, 5081–5099 (2007).
62. Neethu, C. & Abish, B. Climate variability and heat wave dynamics in india: insights from land-atmospheric interactions. *Dyn. Atmos. Oceans* **110**, 101537 (2025).
63. Lekshmi, S. & Chattopadhyay, R. Modes of summer temperature intraseasonal oscillations and heatwaves over the Indian region. *Environ. Res. Clim.* **1**, 025009 (2022).
64. Branstator, G. Circumglobal teleconnections, the jet stream waveguide, and the North Atlantic Oscillation. *J. Clim.* **15**, 1893–1910 (2002).
65. Lin, L. et al. Atlantic origin of the increasing Asian westerly jet interannual variability. *Nat. Commun.* **15**, 2155 (2024).
66. Li, J. et al. Evaluation of CMIP6 global climate models for simulating land surface energy and water fluxes during 1979–2014. *J. Adv. Model. Earth Syst.* **13**, e2021MS002515 (2021).
67. Qiao, L., Zuo, Z. & Xiao, D. Evaluation of soil moisture in CMIP6 simulations. *J. Clim.* **35**, 779 – 800 (2022).
68. De Hertog, S. J. et al. The biogeophysical effects of idealized land cover and land management changes in Earth system models. *Earth Syst. Dyn.* **14**, 629–667 (2023).
69. Davini, P. & D'Andrea, F. From CMIP3 to CMIP6: Northern Hemisphere atmospheric blocking simulation in present and future climate. *J. Clim.* **33**, 10021 – 10038 (2020).
70. Runge, J. et al. Identifying causal gateways and mediators in complex spatio-temporal systems. *Nat. Commun.* **6**, 1–10 (2015).

71. Di Capua, G., Tyrlis, E., Matei, D. & Donner, R. V. Tropical and mid-latitude causal drivers of the eastern Mediterranean Etesians during boreal summer. *Clim. Dyn.* **62**, 9565–9585 (2024).
72. Seneviratne, S. I. et al. Investigating soil moisture–climate interactions in a changing climate: a review. *Earth-Sci. Rev.* **99**, 125–161 (2010).
73. Hong, X., Lu, R. & Li, S. Amplified summer warming in Europe–West Asia and Northeast Asia after the mid-1990s. *Environ. Res. Lett.* **12**, 094007 (2017).
74. Zhang, T. et al. Interannual variability of springtime extreme heat events over the southeastern edge of the Tibetan Plateau: role of a spring-type circumglobal teleconnection pattern. *J. Clim.* **34**, 9915–9930 (2021).
75. Shepherd, T. G. Atmospheric circulation as a source of uncertainty in climate change projections. *Nat. Geosci.* **7**, 703–708 (2014).
76. Lohmann, R., Purr, C. & Ahrens, B. Northern Hemisphere atmospheric blocking in CMIP6 climate projections using a hybrid index. *J. Clim.* **37**, 6605 – 6625 (2024).
77. Fen-ying, C., Cai-hong, L., Song, Y., Kai-qiang, D. & Jürgen, K. Linkage between European and East Asian heatwaves on synoptic scales. *Journal of Tropical Meteorology* **30** (2024).
78. Benson, D. O. & Dirmeyer, P. A. The soil moisture–surface flux relationship as a factor for extreme heat predictability in subseasonal to seasonal forecasts. *J. Clim.* **36**, 6375 – 6392 (2023).
79. Blackport, R. & Fyfe, J. C. Climate models fail to capture strengthening wintertime North Atlantic jet and impacts on Europe. *Sci. Adv.* **8**, eabn3112 (2022).
80. Hersbach, H. et al. The ERA5 global reanalysis. *Q. J. R. Meteorol. Soc.* **146**, 1999–2049 (2020).
81. Mauritsen, T. et al. Developments in the MPI-M Earth System Model version 1.2 (MPI-ESM1. 2) and its response to increasing CO<sub>2</sub>. *J. Adv. Model. Earth Syst.* **11**, 998–1038 (2019).
82. O’Neill, B. C. et al. The scenario model intercomparison project (ScenarioMIP) for CMIP6. *Geosci. Model Dev.* **9**, 3461–3482 (2016).
83. Volodire, A. et al. Evaluation of cmip6 deck experiments with cnrm-cm6-1. *J. Adv. Model. Earth Syst.* **11**, 2177–2213 (2019).
84. Sellar, A. A. et al. UKESM1: description and evaluation of the UK Earth System Model. *J. Adv. Model. Earth Syst.* **11**, 4513–4558 (2019).
85. Hausfather, Z. & Peters, G. P. Emissions-the ‘business as usual’ story is misleading. *Nature* **577**, 618–620 (2020).
86. Pai, D., Srivastava, A. & Nair, S. A. Heat and cold waves over India. in *Observed climate variability and change over the Indian Region*, 51–71 (Springer Singapore, 2017).
87. Perkins, S. & Alexander, L. On the Measurement of Heat Waves. *J. Clim.* **26**, 4500 – 4517 (2013).
88. Russo, S. et al. Magnitude of extreme heat waves in present climate and their projection in a warming world. *J. Geophys. Res. Atmos.* **119**, 12,500–12,512 (2014).
89. Schär, C. et al. The role of increasing temperature variability in European summer heatwaves. *Nature* **427**, 332–336 (2004).
90. Hansen, J., Sato, M. & Ruedy, R. Perception of climate change. *Proc. Natl. Acad. Sci. USA* **109**, E2415–E2423 (2012).
91. Banerjee, A. et al. Recurrence analysis of extreme event-like data. *Nonlinear Process. Geophys.* **28**, 213–229 (2021).
92. Ozturk, U., Malik, N., Cheung, K., Marwan, N. & Kurths, J. A network-based comparative study of extreme tropical and frontal storm rainfall over Japan. *Clim. Dyn.* **53**, 521–532 (2019).
93. Donges, J. F., Zou, Y., Marwan, N. & Kurths, J. Complex networks in climate dynamics: comparing linear and nonlinear network construction methods. *Eur. Phys. J. Spec. Top.* **174**, 157–179 (2009).
94. Boers, N. et al. The South American rainfall dipole: A complex network analysis of extreme events. *Geophys. Res. Lett.* **41**, 7397–7405 (2014).
95. Stolbova, V., Martin, P., Bookhagen, B., Marwan, N. & Kurths, J. Topology and seasonal evolution of the network of extreme precipitation over the Indian subcontinent and Sri Lanka. *Nonlinear Process. Geophys.* **21**, 901–917 (2014).
96. Banerjee, A. et al. Spatial coherence patterns of extreme winter precipitation in the US. *Theor. Appl. Climatol.* **152**, 385–395 (2023).
97. Gupta, S., Boers, N., Pappenberger, F. & Kurths, J. Complex network approach for detecting tropical cyclones. *Clim. Dyn.* **57**, 3355–3364 (2021).
98. Runge, J. Causal network reconstruction from time series: from theoretical assumptions to practical estimation. *Chaos Interdiscip. J. Nonlinear Sci.* **28**, 075310 (2018).
99. Runge, J., Nowack, P., Kretschmer, M., Flaxman, S. & Sejdinovic, D. Detecting and quantifying causal associations in large nonlinear time series datasets. *Sci. Adv.* **5**, eaau4996 (2019).
100. Benjamini, Y. & Hochberg, Y. Controlling the false discovery rate: a practical and powerful approach to multiple testing. *J. R. Stat. Soc. Ser. B* **57**, 289–300 (1995).

## Acknowledgements

The authors would like to thank Dr. Linus Magnusson and Dr. Florian Pappenberger from ECMWF, Reading, UK, and Dr. Armin Köhl from University of Hamburg, Germany, for useful discussions at the conceptual stage of the work. A.B. acknowledges support from the EARTH<sup>RA</sup> project funded by the Deutsche Forschungsgemeinschaft through Reinhart Koselleck projects. S.G. and J.K. were supported by the CAFE project during the conceptual stages of the work, which had received funding from the European Union’s Horizon 2020 research and innovation program under the Marie Skłodowska Curie Grant Agreement No. 813844. S.G. also acknowledges the support of the RESCUE project during the writing of the article, which has received funding from the European Union’s Horizon Europe research and innovation program under Grant Agreement No. 101056939. D.G. was supported by the Science and Engineering Research Board (SERB), Government of India (Project No. CRG/2021/005894). We acknowledge the use of the Tigramite Python package (<https://jakobrunge.github.io/tigramite/>) for causal inference analysis.

## Author contributions

A.B. and S.G. conceptualized the research idea and designed the study. They also led the formal analysis and interpretation of the results. P.P. and A.K. conducted the preliminary investigation. S.G. took the lead in writing the manuscript, including drafting and finalizing it. J.K., C.H., and T.C. contributed by discussing the methodology and providing valuable comments to refine the study. J.K., C.H., and D.G. provided joint supervision throughout the study. All authors contributed to the discussion of the results and participated in the preparation and revision of the final manuscript. J.K. secured the financial support for the project that led to this publication.

## Competing interests

The authors declare no competing interests.

## Additional information

**Supplementary information** The online version contains supplementary material available at <https://doi.org/10.1038/s41612-025-01146-1>.

**Correspondence** and requests for materials should be addressed to Abhirup Banerjee, Shraddha Gupta, Tanujit Chakraborty or Jürgen Kurths.

**Reprints and permissions information** is available at <http://www.nature.com/reprints>

**Publisher’s note** Springer Nature remains neutral with regard to jurisdictional claims in published maps and institutional affiliations.

**Open Access** This article is licensed under a Creative Commons Attribution-NonCommercial-NoDerivatives 4.0 International License, which permits any non-commercial use, sharing, distribution and reproduction in any medium or format, as long as you give appropriate credit to the original author(s) and the source, provide a link to the Creative Commons licence, and indicate if you modified the licensed material. You do not have permission under this licence to share adapted material derived from this article or parts of it. The images or other third party material in this article are included in the article's Creative Commons licence, unless indicated otherwise in a credit line to the material. If material is not included in the article's Creative Commons licence and your intended use is not permitted by statutory regulation or exceeds the permitted use, you will need to obtain permission directly from the copyright holder. To view a copy of this licence, visit <http://creativecommons.org/licenses/by-nc-nd/4.0/>.

© The Author(s) 2025